



The Incorporation of VO_x in the Glass Structure of Electric Arc Furnace Slag and Its Implication on Slag Valorization

Anton Andersson^{1,2} · Min Joo Lee² · Sung Hwan Park² · Su Min Hwang² · Fredrik Engström¹ · Joo Hyun Park²

Received: 26 November 2025 / Accepted: 25 April 2026
© The Author(s) 2026

Abstract

The transition of the ore-based steel industry will increase the global volumes of electric arc furnace (EAF) slag and introduce new components inherently associated with iron ore. For example, vanadium is expected to partition to the slag, and its implications on downstream slag valorization must be considered. Therefore, the present study addressed the effect of VO_x concentration on characteristics relevant to valorization as a supplementary cementitious material (SCM). A synthetic water-granulated $CaO-SiO_2-MgO-Al_2O_3-FeO_x-VO_x$ slag system was systematically varied in VO_x . By incorporating VO_x , the saturation of the divalent metal oxide solid solution (RO-phase) and crystallization of spinel were promoted. Furthermore, dicalcium silicate crystallized at higher temperatures, which suggested an overall greater tendency for crystallization with increasing VO_x concentrations. The effect of adding VO_x on the vitrified fraction of the slag was studied by Raman spectroscopy, indicating that vanadium was incorporated into network-forming structures, but still had a net depolymerizing effect. By standardized SCM reactivity testing, VO_x concentration was found to improve the inherent reactivity of the slag, which was suggested to stem from the depolymerization and the fact that vanadium is not expected to introduce internal diffusion barriers upon slag particle dissolution. Consequently, incorporating VO_x into future EAF slags should be further investigated for environmental aspects as the reactivity was not negatively affected.

Graphical Abstract



Keywords Electric arc furnace slag · Vanadium oxide · Slag structure · Slag valorization · Supplementary cementitious material

The contributing editor for this article was Hiromichi Takebe.

Extended author information available on the last page of the article

Introduction

The decarbonization of the ore-based steel industry may disrupt the established industrial symbiosis with the cement sector [1]. While global blast furnace (BF) capacity is projected to increase [2], regional transitions toward hydrogen-direct reduced iron (H-DRI) and electric smelting could result in local shortages of supplementary cementitious materials (SCMs), especially BF slag [1]. At the same time, electric arc furnace (EAF) slag volumes are expected to rise as decarbonization projects advance [2], thereby justifying a reassessment of their valorization routes. At present, EAF slags are predominantly utilized in road construction [2–4]; however, redirecting their use toward SCM applications could extend the benefit of valorization beyond raw material efficiency to contributing directly to carbon abatement in the cement industry [5].

Five main properties dictate the performance of SCMs in general. Firstly, crystalline materials, with few exceptions, are considered inert [6–8], i.e., an amorphous phase is a prerequisite. Furthermore, by depolymerizing the amorphous phase, the reactivity of the SCM increases [9–12], which can be related to the higher fraction of ionic bonds and a subsequent lower activation energy to hydrolyze these bonds at high pH values [12]. For slags, a caveat is introduced since network modifiers can have low solubility in alkaline environments, which is evident when depolymerization occurs by, e.g., iron oxide [13]. Thus, the chemical composition of the amorphous phase, which is recognized as the third parameter for performance [9, 14], in combination with the degree of polymerization, must be considered. Generally, a higher release of aluminum and silicon in dissolution experiments in alkaline environments has been shown to correlate positively with reactivity [14]. Additionally, the specific surface area of the milled SCM has been identified as a positive driver for increased reactivity since the reactions are surface reactions and larger surface areas provide additional sites for nucleation and growth of reaction products [9, 14, 15]. Lastly, the thermal history has been shown to correlate with reactivity [9, 16, 17].

In reference to the above, the valorization of EAF slags as SCMs requires rapid cooling through granulation. Studies demonstrate that granulated EAF slags show favorable reactivities [18–20], whereas slowly cooled or otherwise crystalline slags exhibit little to no, or at best, reduced performance [21–28]. Research on granulated slags has so far focused mainly on engineered compositions [18–20], which enhance the glass-forming ability and reactivity. While modification strategies are valuable for advancing this valorization route, the comparison between a nonmodified granulated EAF slag

and its engineered counterpart indicated that the former could achieve reactivities comparable to established SCMs [20]. Thus, since omitting hot-stage modification eliminates the need for a separate reaction vessel, this route merits investigation in parallel with ongoing modification efforts [29].

For the valorization of nonmodified EAF slag, compositional variations may occur within a single plant, especially in the context of transitioning to H-DRI. The scrap-to-H-DRI ratio will generate a range of possible concentrations of oxides inherently associated with each iron-bearing material. This is evident from the differences observed between conventional scrap-based EAF slags and those produced in pilot-plant EAF trials using H-DRI [30]. In particular, H-DRI derived from vanadium-containing pellets results in noticeable vanadium pick-up in the slag [30]. Since certain iron ore deposits, such as those in Sweden, contain vanadium oxide incorporated into the iron-bearing minerals [31], this vanadium cannot be removed through conventional mineral processing. Consequently, its transfer to EAF slag and the implications for subsequent slag valorization warrant detailed investigation.

The influence of vanadium on the performance of EAF slags as SCMs has not yet been systematically studied. Nevertheless, data are available on the incorporation of vanadium oxide into systems relevant to metallurgical slags [32–41] as well as into various glass systems [42–61]. Such studies are relevant to SCM performance, as they provide insight into the structural characteristics of the vitrified slag. Vanadium exhibits multiple valence states, with V^{2+} , V^{3+} , V^{4+} , and V^{5+} most commonly observed in slags and glasses [32–47, 54–58, 61]. Moreover, in systems representing slags, multiple valence states have been shown to coexist, with their relative distribution governed by a redox balance influenced by oxygen partial pressure, slag composition, and temperature [32–41].

In addition to the valence distribution, each oxidation state has different preferred coordination numbers [42–61], which can be related to different structural roles [43, 45–59]. Using the concept of cationic field strength (CFS), Lu et al. [46] summarized that the tendency for vanadium to act as a network former increases with higher valence state and lower coordination number. Consequently, as both basicity and partial pressure of oxygen affect the valence distribution, the overall slag composition influences the structural role of vanadium in the system, which is outlined in the following, supported by experimental data from glass systems due to the lack of data for slags.

Octahedrally coordinated $V^{3+}O_6$ has been reported in aluminosilicate glasses [54], and this structural unit has the lowest CFS of reported ionic configurations of vanadium oxide, making it the structural unit most likely to behave as a network modifier [46]. However, in the studied glasses,

the valence distribution toward V^{3+} was low, and no structural role was appointed [54]. Furthermore, V^{4+} has been assigned the coordination as $V^{4+}O_5$ [44, 61] and $V^{4+}O_6$ [42, 47, 56–58] in various glass systems, where $V^{4+}O_5$ was not assessed for its structural implication, and $V^{4+}O_6$ was suggested to be a network modifier [47, 56–58]. Based on the CFS, both behave as intermediates, although $V^{4+}O_5$ has a more network-forming character [46].

Lastly, in glasses containing V^{5+} , the valence has been reported in three different coordination numbers: tetrahedral coordination $V^{5+}O_4$ [44, 45, 48–52, 55, 60, 61], fivefold coordination $V^{5+}O_5$ [43, 47–53, 55, 59–61], and octahedral coordination $V^{5+}O_6$ [45]. Additionally, both $V^{5+}O_4$ and $V^{5+}O_5$ have been reported to be present simultaneously [48–52, 55, 60, 61] and their distribution has been reported to favor fivefold coordination for higher concentrations of V^{5+} [48, 50, 55] and fourfold coordination with increasing presence of network modifiers [49, 50, 52] in their respective glass system. Altogether, the calculated CFS of each V^{5+} unit classifies as a network former [46], but the experimental data show ambiguous results since the reviewed glasses include systems spanning from phosphates to borosilicates. For the latter, low concentrations of V^{5+} have been reported to depolymerize the borate network, but not the silicate network [43, 52]. In phosphate glasses, the introduction of V^{5+} has been shown to depolymerize the glass at low concentrations, and then polymerize the glass at higher concentrations [42, 45, 53, 59]. In other systems, of which the aluminosilicate system reported by Cicconi et al. [54] is the most relevant for the slags considered in the present paper, both $V^{5+}O_4$ and $V^{5+}O_5$ have been attributed as network formers [47, 49, 50, 54].

Based on the above literature review, the total vanadium oxide concentration can be expected to change the structure of EAF slag, and its structural effect would depend on the overall slag composition and the partial pressure of oxygen at which it was generated. Subsequently, this structural change in the molten stage could translate to the vitrified slag structure after water granulation, and consequently, the inherent reactivity of the slag as an SCM. This has not been considered in systematic ways in previously reported research, and therefore, the present paper set out to address these aspects in the synthetic $CaO-SiO_2-MgO-Al_2O_3-FeO_x-VO_x$ system representing EAF-type slag compositions.

Methodology

Slag Design and Synthesis

Five slags were designed within the $CaO-SiO_2-MgO-Al_2O_3-FeO_x-VO_x$ system, where FeO_x and VO_x were added as FeO and V_2O_3 , respectively. Although vanadium was added as V_2O_3 , redistribution of oxidation states during synthesis warrants the use of the term VO_x when referring to vanadium in the slag phase. This terminology is employed throughout this study, except where compositions are reported, in which case values are expressed as V_2O_3 for consistency. The slag composition, listed in Table 1, are in line with those reported for pilot-plant EAF slags generated from H-DRI operation [30], but extended in the total VO_x content to produce a compositional series. The MgO concentration was adjusted to ensure that periclase was the primary crystallizing phase, without being excessively high as to raise the liquidus temperature substantially. This assessment was made by thermodynamic calculations in the “Equilib” module of FactSage (Ver. 8.3) thermochemical computing software, employing the FToxid and FactPS databases [62].

As the slag design aimed at additions of ferrous oxide, synthetic FeO was produced from a stoichiometric mixture of reagent-grade Fe and Fe_2O_3 . The synthesis was performed in a graphite resistance-heated furnace (Ruhstrat, Göttingen, Germany), illustrated in Fig. 1. The stoichiometric mixture was heated in an iron crucible at 10 K/min to 1173 K, held for 5 h, and cooled with the furnace. An inert atmosphere was maintained throughout by flowing Ar (99.999%) and N_2 (99.996%) at flow rates of 3 and 12 L/min, respectively. The heating cycle was repeated after milling, and the absence of Fe_3O_4 and Fe_2O_3 was confirmed by X-ray diffraction (XRD) using a Panalytical Empyrean X-ray diffractometer with $Cu K\alpha$ radiation generated at 45 kV and 40 mA.

The compositions in Table 1 were mixed using the reagent-grade chemicals $CaCO_3$, SiO_2 , MgO , Al_2O_3 , and V_2O_3 , as well as the produced FeO . Each slag was synthesized in yttria-stabilized MgO crucibles (98.5% $MgO + Y_2O_3$; Tateho Ozark Technical Ceramics Inc.) under the same inert conditions as previously accounted for using the experimental setup presented in Fig. 1. The temperature was ramped to the

Table 1 Design compositions [wt%] and calculated liquidus temperature [K]

Slag	CaO	SiO ₂	MgO	Al ₂ O ₃	FeO	V ₂ O ₃	Liquidus T
V0	39.3	19.7	6.0	5.0	30.0	0.0	1785
V1	38.3	19.2	6.0	5.0	30.0	1.5	1772
V2	37.3	18.7	6.0	5.0	30.0	3.0	1760
V3	36.3	18.2	6.0	5.0	30.0	4.5	1747
V4	35.3	17.7	6.0	5.0	30.0	6.0	1734

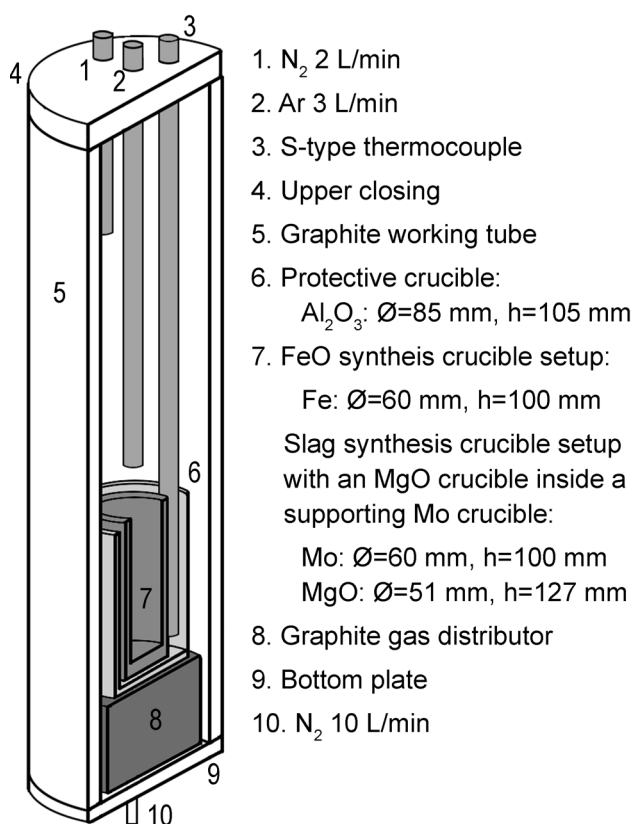


Fig. 1 Schematic overview of the experimental setup, including crucible configurations, used for the synthesis of FeO and slags

slags' respective calculated liquidus temperature at a rate of 10 K/min. After homogenization during an isothermal hold of 1 h, the temperature was ramped to 100 K superheating at a rate of 10 K/min. Upon reaching the final temperature, the slag was removed manually from the furnace and granulated in water jets using the procedure accounted for in a previous publication [20]. The onset of granulation was commenced within 15 s of removing the slag from the furnace. The heating cycle was designed to achieve sufficient homogenization without causing excessive MgO dissolution. Furthermore, applying 100 K superheating prior to granulation minimizes unintended thermal history effects in the subsequent reactivity testing of the slags.

Chemical Composition and Iron Valence Distribution

The slags were fused with reagent-grade Na₂CO₃ and H₃BO₃, dissolved in HCl, and analyzed for their bulk chemical compositions by inductively coupled plasma-optical emission spectroscopy (ICP-OES) using a SPECTRO ARCOS ICP-OES analyzer (SPECTRO Analytical Instruments, Kleve, Germany). Automatic cerimetric titration

with Ce(SO₄)₂ in HCl was employed to determine the iron valence distribution.

Mineralogical Composition

The mineralogical composition was determined by powder XRD using the Panalytical Empyrean X-ray diffractometer, as detailed above. To estimate the amorphous fraction, scans were performed on slags mixed with 10 wt% reagent-grade corundum (Al₂O₃) as an internal standard. These scans were performed using Cu K_α radiation (45 kV, 40 mA) over 10–90°2θ with a step size of 0.0130°2θ and a scan step time of 998 s. Phase identification and Rietveld refinement were carried out with HighScore + software using the FIZ Karlsruhe Inorganic Crystal Structure Database [63, 64].

Slag Granule Characteristics

Scanning electron microscopy with energy dispersive X-ray spectroscopy (SEM-EDS) was utilized to assess the granule morphology and microstructure, and to estimate the chemical composition of phases. Each sample was mounted in epoxy, polished using standard metallographic procedures, and carbon-coated. The analyses were performed using a Zeiss Merlin field emission SEM (Carl Zeiss AG, Oberkochen, Germany) equipped with a silicon drift EDS detector (Oxford Instruments, Abingdon, UK).

Slag Structure

Micro-Raman spectroscopy was performed on glassy regions of slag granules to assess the effect of VO_x concentration on the long-range order slag structure in a molecular dimension. Spectra were collected using a LabRAM Aramis Raman microscope (Horiba Jobin Yvon, Kyoto, Japan) with a 514 nm excitation wavelength by Ar laser. A semi-quantitative Gaussian deconvolution of the Raman spectra was carried out referencing literature data using PeakFit v4.12.

Milling and Specific Surface Area Measurements

Each slag was milled using a FRITSCH Pulverisette 7 planetary ball mill equipped with 45 mL tungsten carbide grinding bowls (FRITSCH GmbH, Idar-Oberstein, Germany). The milling was carried out at 600 revolutions per minute (rpm) with 18 tungsten carbide balls of 10 mm in diameter using a ball-to-slag mass ratio of 10.5. The milled slags were characterized for their specific surface

areas by the Brunauer–Emmet–Teller (BET) method using a Micromeritics Gemini 2390a after degassing at 573 K for 60 min with a Micromeritics FlowPrep 060 (Micromeritics Instruments Corporation, Norcross, GA, USA).

Reactivity Testing

The reactivity of the milled slags as SCMs was assessed using the Rapid Reliable Relevant (R3) isothermal calorimetry-based rapid screening test for SCMs [65, 66], established as method A in the ASTM standard C1897–20. This test was chosen on the basis of the study presented by Li et al. [66], which demonstrated that the R3 test results correlated strongly with the strength of mortars, independent of the type of SCM, and with great repeatability between laboratories. Furthermore, this calorimetry-based method tests the inherent reactivity of the SCM without the influence of cement hydration [67, 68]. In the tests of the present study, a TAM Air isothermal calorimeter (TA Instruments, New Castle, DE, USA) was used.

Results and Discussion

Chemical and Mineralogical Composition

The chemical compositions of the synthesized slags are presented in Table 2. Overall, the target compositions were closely reproduced, with only minor and systematic deviations. For example, B2 basicity (i.e., Vee ratio, CaO/SiO₂) was slightly higher than intended, and a partial substitution of crucible MgO for iron oxide was evident. Furthermore, although evaporation [37] lowered the final vanadium contents relative to the design, the synthesized slags achieved the aim of producing a series in which VO_x was the principal compositional variable.

In addition to the ICP-OES analyses, the slags were analyzed for their Fe³⁺/Fe²⁺ valence distributions by titration, yielding ratios of 4.0–7.0, as presented in Table 2. To offer a reference, equilibrium Fe³⁺/Fe²⁺ ratios were calculated using the Equilib module in FactSage 8.3 [62] with the FToxid and FactPS databases, based on the compositions in Table 2 at the respective final experimental temperature. Assuming an

oxygen partial pressure of 4×10^{-5} atm for 99.996% N₂, the equilibrium Fe³⁺/Fe²⁺ ratios were found to be lower, ranging from 1.1–1.2. Furthermore, from a mass-balance perspective, the available gas during the experiments is insufficient to oxidize Fe²⁺ to Fe³⁺ at the levels indicated by equilibrium. Therefore, the measured Fe³⁺/Fe²⁺ ratios most likely reflect post-furnace oxidation, primarily during water granulation, filtering, and drying.

The X-ray diffractograms presented in Fig. 2 show that the slags underwent crystallization during the water granulation, which is consistent with previous data showing that producing fully amorphous EAF slag is challenging without modification [2, 20]. The crystalline phases detected were largely the same across samples, except for a change in the dicalcium silicate (C₂S) polymorph at the two highest VO_x concentrations. Since α-C₂S is stable at higher temperatures than α'-C₂S [69], this suggests that increasing VO_x contents promoted crystallization. Although the

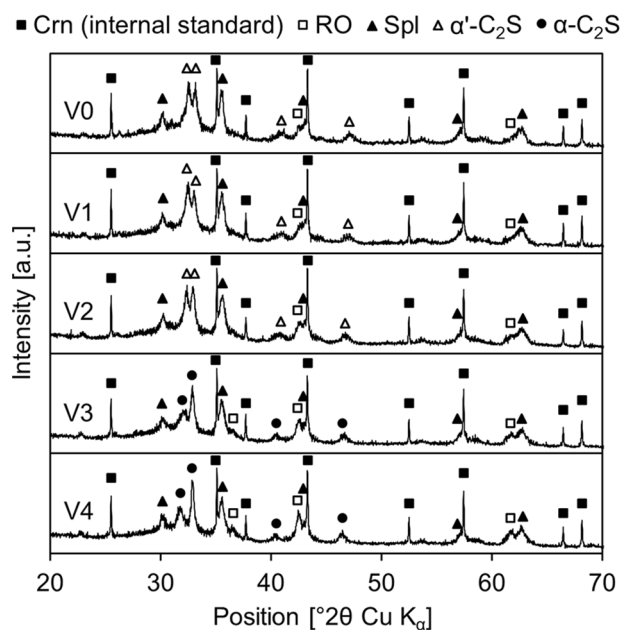


Fig. 2 Diffractograms of the granulated slags with the internal standard. The displayed 2θ range is cropped to enhance the visualization of the main features. Crn=corundum, RO=solid solution phase, Spl=spinel, and C₂S=dicalcium silicate

Table 2 Chemical composition [wt%] with FeO_x and VO_x represented as FeO and V₂O₃, respectively

Slag	B2	CaO	SiO ₂	MgO	Al ₂ O ₃	FeO	V ₂ O ₃	Fe ³⁺ /Fe ²⁺ (analyzed)
V0	2.06	39.9	19.3	7.2	5.1	28.5	0.0	6.6
V1	2.04	39.1	19.2	7.2	5.1	28.4	1.0	7.0
V2	2.05	38.3	18.7	7.3	5.1	28.5	2.0	4.8
V3	2.05	37.7	18.4	7.1	5.1	28.7	3.0	4.0
V4	2.05	37.1	18.0	6.9	5.2	28.8	4.1	4.6

Table 3 Estimated phase distribution [wt%] by Rietveld refinement with internal standard

Slag	Amorphous	RO	Spl	C ₂ S
V0	72.2	4.6	7.6	15.6
V1	73.7	4.1	7.8	14.4
V2	66.9	6.3	10.1	16.7
V3	66.4	11.3	10.5	11.8
V4	67.0	11.1	9.6	12.3

RO solid solution phase, *Spl* spinel, and C₂S dicalcium silicate

fraction of C₂S decreased at the highest VO_x concentration, Table 3 shows a concurrent increase in spinel and divalent metal oxide solid solution (RO phase), identified as magnesioferrite ((Mg,Fe)Fe₂O₄) and MgO-rich magnesiowüstite ((Fe,Mg)O), respectively. The redistribution among crystalline phases results in an overall reduction of the amorphous fraction with increasing VO_x, followed by

a plateau at higher concentrations. The plateau, together with the shift towards the higher-temperature C₂S polymorph, indicates that VO_x promotes crystallization, while the evolving phase assemblage moderates the net decrease in amorphous content.

Granule Characteristics

Micrographs of samples V0 and V4, selected as the extremes of the series, are presented in Fig. 3; the remaining samples are omitted for brevity. The low-magnification images, i.e., Fig. 3a and c, show a granule morphology resulting from mechanical droplet formation followed by rapid cooling. The former produced spherical and ellipsoidal granules, whereas the latter resulted in internal crack propagation and particle breakage due to thermal stress, leading to multiple granule shreds as visible in the micrographs.

The high-magnification micrographs of Fig. 3 were selected from granules with pronounced crystallization.

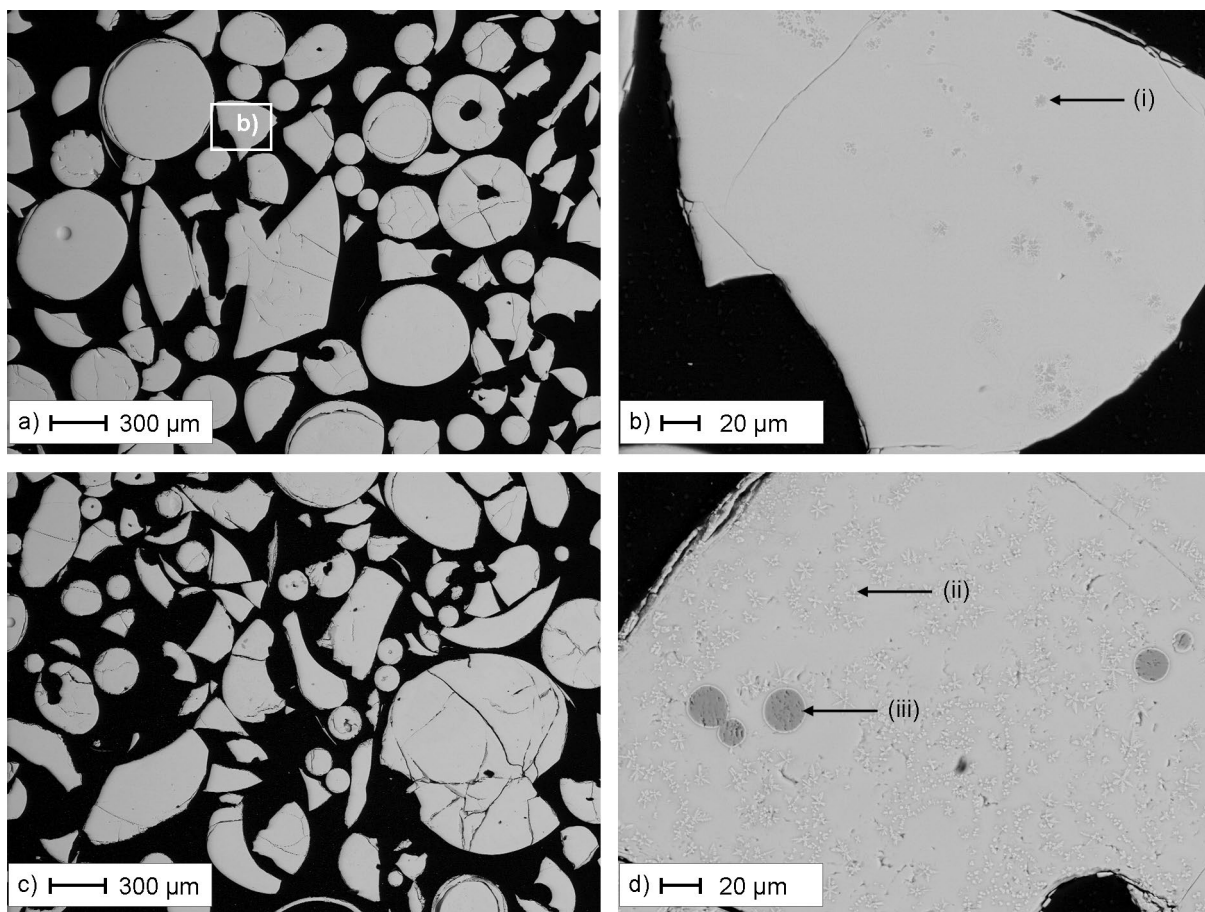


Fig. 3 Low- and high-magnification micrographs of samples: **a** V0, **b** V0, **c** V4, and **d** V4. Phase stoichiometries representing (i) Ca₂SiO₄, (ii) indicated (Mg,Fe)(Al,Fe,V)₂O₄, and (iii) (Mg_{0.8}Fe_{0.2})O. The high-magnification micrograph presented in Fig. **b** is marked by the rec-

tangle in Fig. **a**, whereas the high-magnification micrograph of Fig. **d** was taken outside of the presented area of the low-magnification micrograph in **c**

In general, the microstructure was characterized by a high degree of supercooling, which increased the thermodynamic driving force for nucleation (via a larger difference in volume-specific Gibbs free energy) but demoted growth due to suppressed diffusion. Furthermore, slag V4 was saturated in the RO phase during the synthesis, as evidenced by the morphology of phase (iii) in Fig. 3d. This latter morphology was exclusively found for samples V3 and V4, which is consistent with the Rietveld data presented in Table 3 in terms of abundance. Finally, identification of stoichiometries representing polymorphs of Ca_2SiO_4 was evident, whereas spinel stoichiometries were tentative owing to the possibility of the electron beam's interaction volume entering underlying phases.

The vitrified nature of the slag was apparent from considering the featureless regions in the micrographs, which is especially clear considering Figs. 3b and d. The composition of the amorphous phase was estimated by point analyses using the silicon drift EDS detector, and the results are presented in Fig. 4. Despite differences in crystallization behavior upon VO_x addition, the series incorporated vanadium into the vitrified slag in progressively higher concentrations. The B2 basicity of the glass phase was 2.09, 2.05, 2.00, 2.03, and 1.97 for slags V0, V1, V2, V3, and V4, respectively. As the concentrations of the remaining components were relatively comparable, the slag series was considered suitable for assessing the influence of VO_x on slag structure and reactivity.

VO_x in the Vitrified Slag

Raman spectroscopy was employed to study the structure of the vitrified slag, specifically in relation to the incorporation of VO_x . The Raman spectra of glassy regions of slag granules are presented in Fig. 5. All samples exhibited peaks concentrated in three spectral regions: a low wavenumber range ($410\text{--}590\text{ cm}^{-1}$), a medium range ($590\text{--}800\text{ cm}^{-1}$), and a high range ($800\text{--}1125\text{ cm}^{-1}$). Although the differences in VO_x concentrations between individual samples are minor, variations are apparent when considering the spectra. To interpret these spectral differences, literature data on previously reported vibrational bands of structural units were reviewed, followed by a subsequent Gaussian deconvolution of the spectra.

Considering Fig. 5, the spectrum of V0 in the low wavenumber range exhibited two peaks, of which the Raman band between $410\text{--}487\text{ cm}^{-1}$ was weaker. Previous data have attributed this latter band to the bending vibration of bridging oxygen in Si-O-Si linkages, with specific peak position ranges of $446\text{--}465\text{ cm}^{-1}$ [58, 70, 71]. Furthermore, the Raman band of slightly greater intensity, between wavenumbers $487\text{--}590\text{ cm}^{-1}$, has previously been attributed

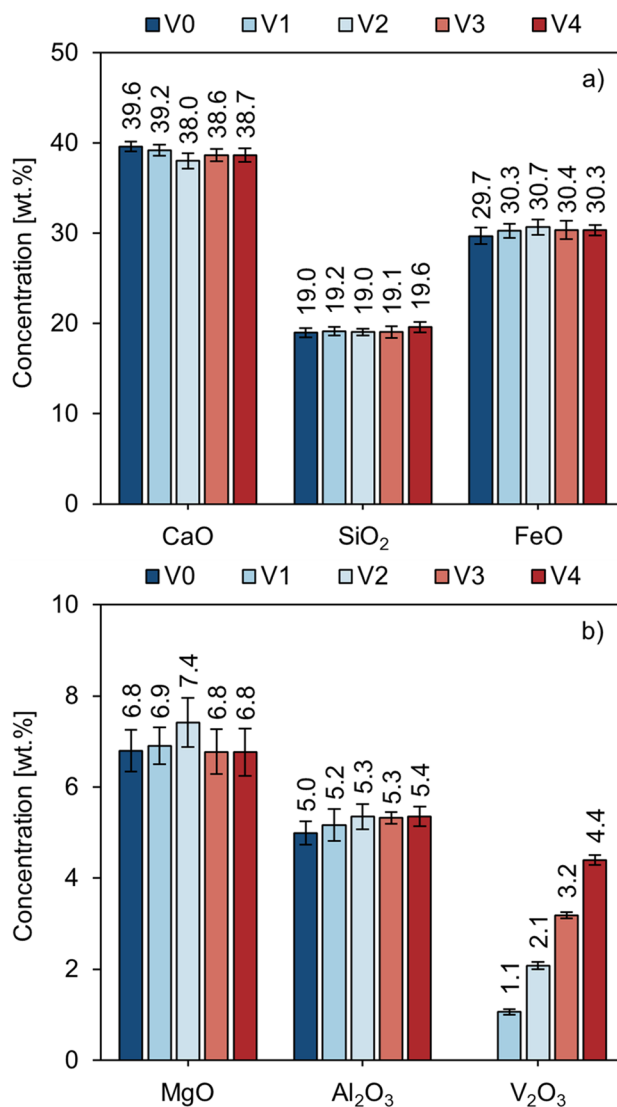


Fig. 4 Estimated composition of vitrified slag based on EDS measurements of ten individual granules: **a** CaO, SiO₂, and FeO, and **b** MgO, Al₂O₃, and VO_x expressed as V₂O₃. Error bars denote the standard deviation of the respective component

to the bending vibration of bridging oxygen in Al-O-Al ($534\text{--}570\text{ cm}^{-1}$) [70, 72–74].

The introduction of VO_x into the system suggests the presence of a third structural entity contributing to the recorded intensity in the low wavenumber region, as is evidenced by the bridging of the two peaks observed in sample V0. Literature data on vanadium have reported the bending vibration of bridging oxygen in V-O-V at $443\text{--}500\text{ cm}^{-1}$ [50, 51, 55, 75, 76] or 524 cm^{-1} [77, 78].

The Raman band in the mid-wavenumber range initially exhibits a slight blue shift upon incorporation of VO_x (see Fig. 5). However, with increasing concentrations of VO_x , a red shift is observed. Again, by first considering the vanadium-free system, literature data assign the

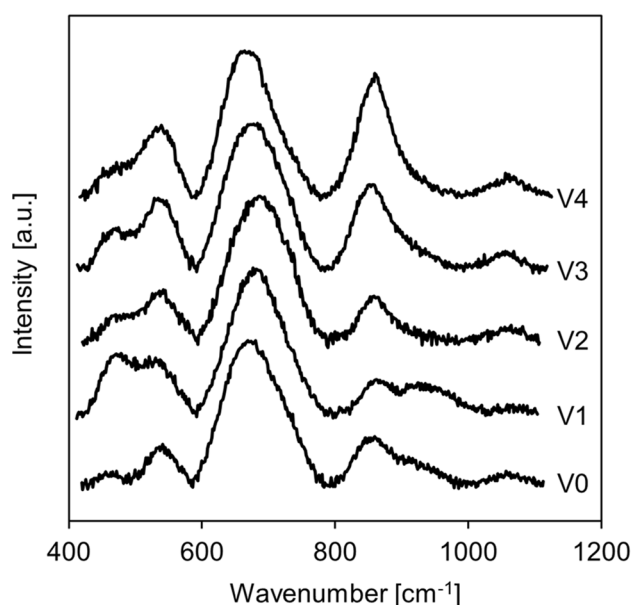


Fig. 5 Raman spectra of glassy regions of slag granules

Fe–O stretching vibration in octahedrally coordinated Fe^{3+} to the range $607\text{--}637\text{ cm}^{-1}$ [70, 79]. For Fe^{3+} in a tetrahedral coordination, i.e., $(\text{FeO}_2)^-$, the corresponding band typically appears at higher wavenumbers, around $640\text{--}693\text{ cm}^{-1}$ [70, 72, 74, 79, 80]. Additionally, the Al–O stretching vibration in tetrahedrally coordinated $(\text{AlO}_2)^-$ units have been attributed to the mid-wavenumber region observed in the present study. The exact band position depends on the nonbridging oxygen by Al ratio (NBO/Al), with Q_{Al}^2 units (NBO/Al = 2) reported in the range of $712\text{--}740\text{ cm}^{-1}$ [70, 72, 74], and Q_{Al}^3 units (NBO/Al = 1) appearing at $739\text{--}790\text{ cm}^{-1}$ [70, 72–74].

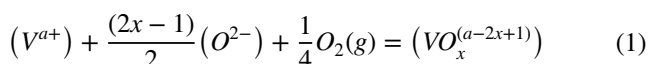
In addition to the possible structural units covered for the vanadium-free system, the incorporation of VO_x introduces additional spectral features in the mid-wavenumber region. Stretching vibrations of threefold coordinated oxygen in V–O–V bridges in crystalline V_2O_5 have been observed at $702\text{--}703\text{ cm}^{-1}$ [81, 82], and comparable bands have been attributed to polymerizing V–O–V bridging oxygen in slags at $690\text{--}710\text{ cm}^{-1}$ [76–78, 83] or various amorphous materials at $661\text{--}715\text{ cm}^{-1}$ [55, 84, 85].

The high wavenumber range, defined as $800\text{--}1125\text{ cm}^{-1}$ in the present study, is generally assigned to the symmetric stretching vibrations of the Q_{Si}^n units, where n indicates the number of bridging oxygens per silicon (NBO/Si). Specifically, the monomer, Q_{Si}^0 , has been attributed to wavenumbers in the range $840\text{--}884\text{ cm}^{-1}$ [76–79, 83, 86–89]. Furthermore, the dimer, Q_{Si}^1 , has been reported in the range $900\text{--}930\text{ cm}^{-1}$, whereas the more polymerized chain (Q_{Si}^2) and sheet (Q_{Si}^3) have been assigned $950\text{--}1015\text{ cm}^{-1}$ and $1020\text{--}1114\text{ cm}^{-1}$, respectively [76–79, 83, 86–89].

The consistently reported spectral features of vanadium in the high wavenumber range include stretching vibrations of the V=O bond in V^{5+}O_4 and V^{5+}O_5 , which have been reported in the ranges $890\text{--}930\text{ cm}^{-1}$ [48, 49, 51–53, 84] and $968\text{--}1021\text{ cm}^{-1}$ [42, 47–51, 55, 59, 81, 82, 84], respectively. Owing to the low energy requirements for changing between the coordination numbers, both forms have been reported to coexist, reported as a broad band between $890\text{--}950\text{ cm}^{-1}$ [48, 50, 51].

By considering the reported bands from the literature, the Gaussian deconvolution of the Raman spectra in Fig. 5 was performed. The deconvoluted spectra are presented in Fig. 6, and all slags were fitted with R^2 values exceeding 0.993. Table 4 presents a summary of the ranges of central peak positions, the corresponding structural representation, and the relative area in the Gaussian deconvolution for all five slags, which was used as the basis for understanding the incorporation and effect of VO_x on the structure of the vitrified portion of the slag samples. As is clear from the data in Table 4, qualitative trends are present when considering the incorporation of VO_x into the slag system, but no clear systematic variation with increasing concentrations can be stated. This could be an effect of the heterogeneous nature of the samples due to the partial crystallization. Nevertheless, the qualitative differences were addressed, as outlined in the following.

Although vanadium was added as V_2O_3 during the slag synthesis, a valence redistribution can be assumed to occur [32–41]. Upon the introduction of vanadium to slags, Farah and Brungs suggested that the redox pair equilibrium follows an O-type reaction, according to Eq. (1), for one electron change between valence states [36].



where, x is the number of oxygen associated with the ion of the oxidized state. However, to accurately describe vanadium valence states, a multivalent redox equilibrium extending beyond a redox pair is necessary to consider [32, 36]. Nevertheless, Eq. (1) effectively shows that the distribution to higher valences is favored by both higher partial pressures of oxygen (p_{O_2}) and oxygen anion activity ($a_{\text{O}^{2-}}$, i.e., basicity), which has been verified experimentally [32–38]. Consequently, considering the comparably high basicity employed in the present study, the redox equilibrium can be assumed to allow an appreciable distribution to higher valence states, which are more likely to act as network formers based on their corresponding CFS [46]. Although Raman spectroscopy cannot be used to quantify vanadium valence states, the suggested valence redistribution is indicated by the data in Table 4, with V–O–V linkages and

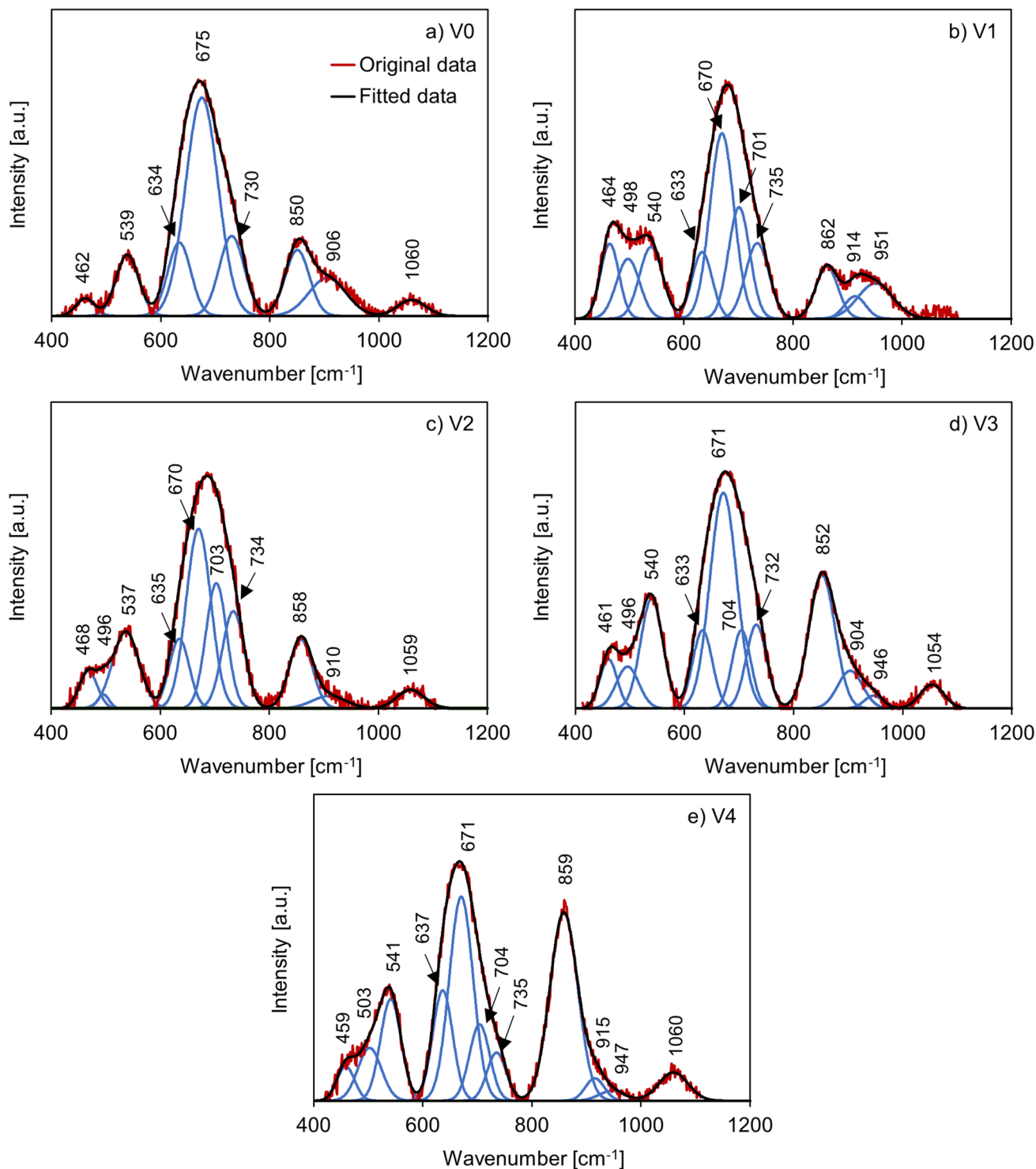


Fig. 6 Deconvoluted Raman spectra of samples **a** V0, **b** V1, **c** V2, **d** V3, and **e** V4

possible V=O bonds. The latter feature has been reported to be present even at low concentrations as double bonds are strong Raman vibrators [61], but it must be acknowledged that the bands overlap with those of the silicate network.

According to Table 4, one of the main features of introducing VO_x was the decrease in the total area attributed to ferric iron. Additionally, adding VO_x indicated a lower ratio of tetrahedral to octahedral ferric iron, i.e., $(\text{FeO}_2)^- / (\text{Fe}^{3+})$, though this observation must be

Table 4 Results of the Gaussian deconvolution of the Raman spectra presented as areas [%] for the assigned structural features and their corresponding ranges of central peak positions

Raman centered shift [cm ⁻¹]	Raman assignment	V0	V1	V2	V3	V4
459–468	Si–O–Si	2	8	4	4	3
496–503	V–O–V (bv)	/	8	1	5	6
537–541	Al–O–Al	9	10	13	12	10
633–637	Fe–O in octahedral Fe ³⁺	11	8	9	8	11
670–675	Fe–O in (FeO ₂) ⁻	44	26	27	29	24
701–704	V–O–V (sv)	/	14	16	7	8
730–735	Al–O in Q _{Al} ²	13	10	13	9	5
850–862	Si–O in Q _{Si} ⁰	10	7	10	17	26
904–915	V=O in V ⁵⁺ O ₄ and/or Si–O in Q _{Si} ¹	9	3	3	5	2
946–951	V=O in V ⁵⁺ O ₅ and/or Si–O in Q _{Si} ²	/	7	/	1	1
1054–1060	Si–O in Q _{Si} ³	3	/	3	3	4

Raman bands for V–O–V are distinguished as bending vibrations (bv) and stretching vibrations (sv).

confirmed by Mössbauer spectroscopy. Although the iron valence titration data presented in section “[Chemical and Mineralogical Composition](#)” were argued primarily to stem from postfurnace oxidation, VO_x appears to influence the Fe³⁺/Fe²⁺ ratio as seen qualitatively for the highest VO_x concentrations in Table 2. Therefore, the intrinsic stability of both vanadium and iron oxides in their pure states was investigated as an indication of their relative stabilities in a multicomponent solution. As shown in Fig. 7, introducing VO_x as V₂O₃ in the slag synthesis can be assumed to partially reduce Fe³⁺, with implications for the slag structure as outlined in the following.

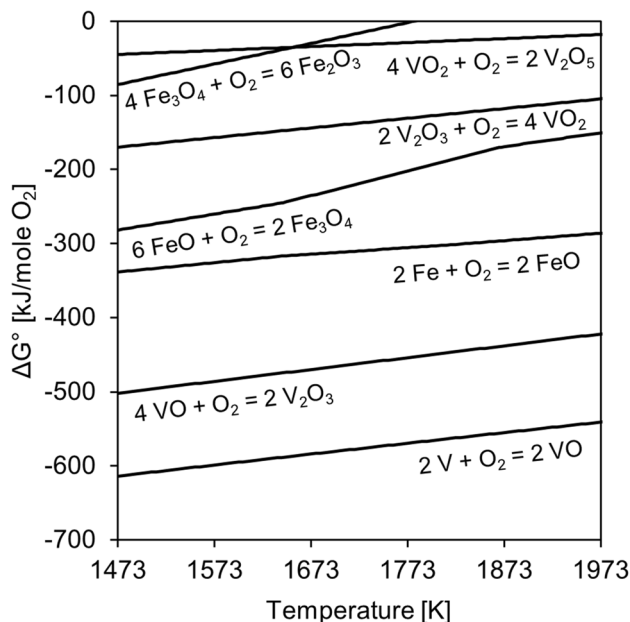
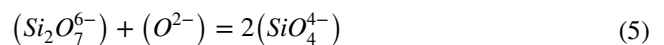
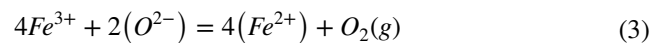
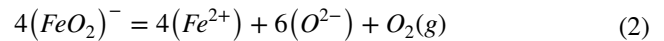


Fig. 7 Ellingham diagram calculated using the Reaction module of FactSage 8.3 using the FactPS database [62]

Mysen and Virgo [90] presented the redox equilibria for tetrahedral and octahedral Fe³⁺ according to Eq. (2) and Eq. (3), respectively. Furthermore, Eq. (4) was introduced to highlight the change from tetrahedral to octahedral coordination of Fe³⁺ [90]. In addition to these equations, the depolymerization of the silicate network can be represented by, e.g., Q_{Si}¹ and Q_{Si}⁰, according to Eq. (5).



This representation suggests that the reduction of tetrahedral Fe³⁺ is associated with a depolymerization of the silicate network. The same is true for shifting tetrahedral to octahedral Fe³⁺. However, if octahedral Fe³⁺ is reduced, the silicate network is polymerized. As shown by Mysen and Virgo [90], the net effect of the competition between Eq. (2) through Eq. (4) can be either polymerizing or depolymerizing.

For the slags of the present study, the addition of VO_x can be assumed to establish a redox equilibrium with iron, resulting in an overall depolymerizing effect, i.e., a net release of (O²⁻) ions. This interpretation is qualitatively supported by the Q_{Si}⁰ data presented in Table 4. Moreover, in iron-rich slags, higher a_{O²⁻} has been shown to promote octahedral coordination of ferric iron [91], which also would act depolymerizing to the slag structure. Finally, although the Raman spectroscopy results indicate that VO_x is associated with bridging oxygens and appears in structural units of higher vanadium valence states, vanadium in lower

oxidation states may still act as network modifiers, as discussed in the literature review in section “Introduction.” Though Raman data cannot be used to assess the valence state distribution of vanadium, this net depolymerizing structural interpretation is consistent with published viscosity data in the $\text{CaO-SiO}_2\text{-MgO-FeO}_x\text{-VO}_x$ system, showing that vanadium oxide decreases the viscosity [92]. Consequently, the higher VO_x concentrations in the present compositional series are in effect associated with higher ionic mobilities in accordance with the Eyring equation (Eq. (6)) [93], which promotes nucleation and growth rates, as evidenced by the higher crystalline contents exhibited by the samples with higher VO_x concentrations as compared with the sample without VO_x , Table 3.

$$D = kT / \lambda\eta \quad (6)$$

where, D is the diffusion coefficient [m^2/s], k is the Boltzmann constant [J/K], T is the temperature [K], λ is the jumping distance [m], and η is the viscosity [Pas].

As the slags investigated in the present study were designed in alignment with compositions reported for pilot-plant EAF slags generated from H-DRI operation [30], the influence of oxygen anion activity on vanadium speciation is expected to be broadly comparable. However, industrial EAF operations involve redox conditions buffered by liquid steel and influenced by foaming practice, leading to oxygen partial pressures that differ from those established under inert laboratory scale experiments. Accordingly, the impact of such industrial partial pressures of oxygen on vanadium speciation and its structural implication warrants further investigation, particularly as vanadium-containing EAF slags have not yet been examined in this regard.

Impact of VO_x on Reactivity

The slags were milled with the aim of producing samples with comparable specific surface areas. Based on the BET measurements, the values ranged from 0.75–0.91 m^2/g (V0: 0.91, V1: 0.77, V2: 0.76, V3: 0.76, V4: 0.75). Thus, slags V1–V4 exhibit closely similar specific surface areas, whereas V0 shows a higher value. Furthermore, the RO phase and spinel are generally considered inert in reactivity measurements [6–8], so their varying concentrations (Table 3) can be neglected. The impact of the C_2S polymorphs on the R3 test is less clear, but the saturated Ca(OH)_2 conditions are expected to limit C_2S 's contribution to the generated heat. However, in a hydration environment, the presence of crystalline C_2S is not necessarily negative for these slags. The amorphous contents are similar across slag V0–V1 and V2–V4 (Table 3), respectively. In conclusion, the reactivity measurements can favor higher reactivities for slag V0 and V1 based on these characteristics, which must

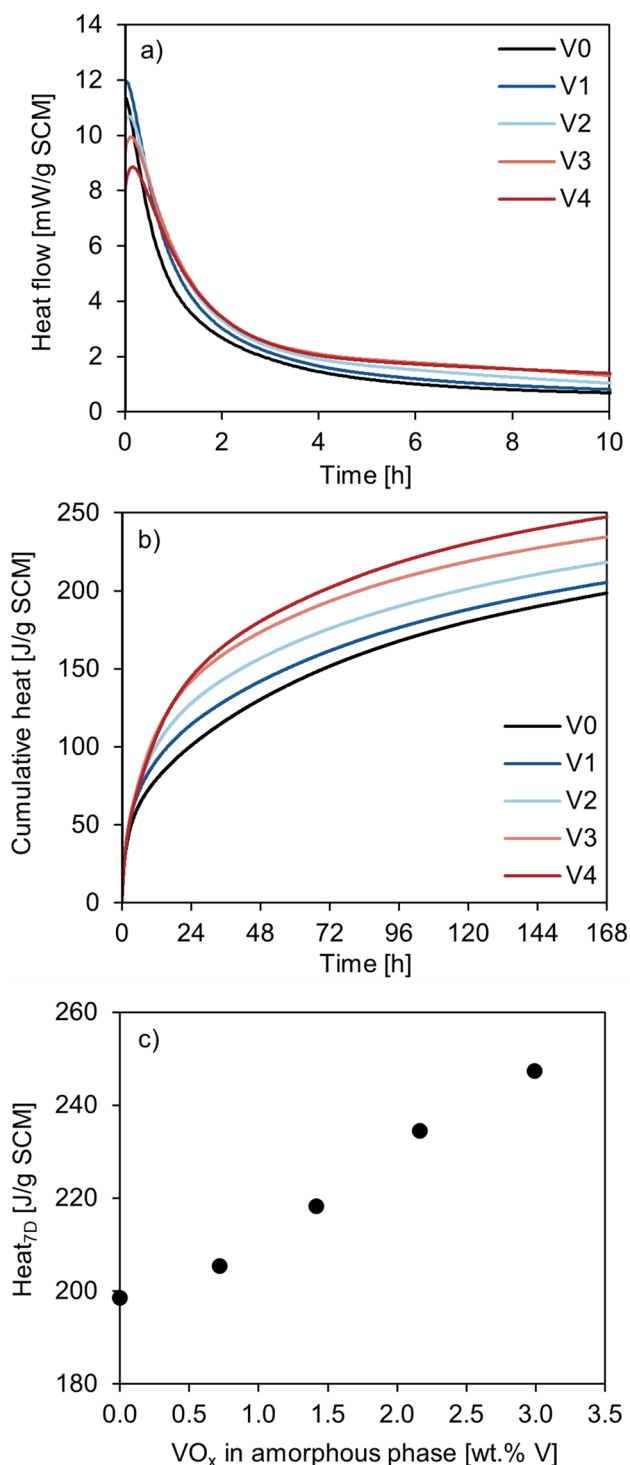


Fig. 8 R3 isothermal calorimetry-based test results showing **a** heat flow during the first 10 h, **b** cumulative heat for 7 days, and **c** cumulative heat after 7 days versus VO_x in the amorphous phase estimated by EDS

be kept in mind when assessing the reactivity data for the impact of VO_x concentration and structure of the vitrified slag.

The heat flow during the first 10 h of the R3 isothermal test is presented in Fig. 8a. For V0, the recorded heat flow at the beginning of the data acquisition was already decreasing, indicating that the maximum heat flow likely occurred during the calorimeter stabilization period. With each subsequent increase in VO_x concentration, the peak maximum shifted approximately 2 min. In addition, the maximum heat flow consistently decreased, with values of 12.0, 10.7, 9.9, and 8.9 mW/g SCM for slags V1, V2, V3, and V4, respectively. On the descending flank of the peaks, the heat flow curves diverged within 8 h of the test, with V4 showing the highest values, followed by V3, V2, V1, and V0. This inherent order was maintained for the majority of the experiment, resulting in a progressively higher cumulative heat release with increasing VO_x concentration, as presented in Fig. 8b and highlighted in Fig. 8c.

The underlying mechanism remains to be clarified and requires dedicated experimental investigation. Two potential contributing factors can be hypothesized: (i) the solubility of vanadium in alkaline conditions relevant to the R3 test [94, 95], and the subsequent depletion of supersaturated vanadium through precipitation of calcium vanadate [96], which suggests that vanadium does not form a diffusion barrier within the slag particle; and (ii) an increase in the average ionic fraction of the cation–oxygen bonds in the vitrified slag, thereby reducing bond strength and enhancing their susceptibility to hydrolysis in alkaline environments [12]. This second mechanism is supported by the net depolymerizing effect outlined in the structural investigation of section “ VO_x in the Vitrified Slag.”

Compared with previously reported modified and nonmodified EAF slags assessed for use as SCMs [18–20], the present compositional series was designed to isolate the effect of VO_x rather than to maximize glass formation and reactivity. Nevertheless, benchmarking against established SCMs such as siliceous fly ash and ground granulated blast furnace slag (GGBS) provides a useful baseline for assessing the performance of the present slags. In this context, the reactivity of the studied slags is more comparable to that of fly ash than to GGBS, with reported values of 163–214 [66] and 504–559 J/g SCM [20, 66], respectively. Considering the isolated effect of VO_x , the results of V0–V4 show that increasing VO_x concentrations depolymerizes the slag structure and enhances inherent reactivity despite a reduction in amorphous fraction. Previous data have shown that increased depolymerization is associated with higher early heat release in inherent reactivity testing; however, within a 7-day measurement window, the higher amorphous fraction achieved through silica modification can exert a stronger influence on cumulative heat than structural depolymerization alone [20]. As the present compositional series induces structural changes without simultaneous introduction of a conventional pozzolanic modifier, e.g.,

silica, the investigated VO_x compositional window did not generate clearly competing mechanisms governing reactivity.

Based on the above, for the valorization of EAF slag as an SCM within the framework of varying scrap-to-H-DRI ratios, the potential performance decrease associated with VO_x incorporation into the vitrified slag does not constitute a concern. Nevertheless, additional testing on blended cement systems, specifically compressive strength testing using mortars, is recommended for verification. Furthermore, although the current experimental setup has been shown to generate industrially relevant data for iron silicate slags [97], the industrial relevance for EAF slags should be pursued in future studies, examining the correspondence between water-granulated slags generated in laboratory and industrial-scale settings.

Consequently, the primary concern associated with vanadium could be environmental rather than reactivity-related. Regulatory frameworks differ between countries, with some focusing on bulk concentrations of metals in the slag, while others emphasize leaching behavior under application-specific conditions [2]. In the case of vanadium, bulk concentrations must be adhered to when applied, whereas leaching behavior must be evaluated within the intended application context. As the behavior of vanadium in vitreous slags as SCMs has not yet been addressed in the literature, indicative insights can be drawn from clinker. Studies show that vanadium can become immobilized within the concrete matrix after prolonged curing, reducing its release, though not to levels that would classify it as inert [98–101]. Given that the vanadium concentrations in clinkers are generally lower than those expected in EAF slags, detailed investigations of vanadium behavior in vitreous SCM systems are required. Regulatory limits for vanadium leaching vary between countries, including within the European Union [2, 101]. In some jurisdictions, no specific regulatory thresholds for vanadium are defined, in which case comparison with maximum concentration levels for groundwater may be considered a conservative reference [98]. For example, standardized leaching criteria applied to steelmaking slags used as aggregates have reported limits of 250 $\mu\text{g/L}$ [4], which are aligned with groundwater quality guideline values [98]. Accordingly, compliance for SCM applications would ultimately need to be verified through dedicated leaching assessments under the relevant regulatory framework.

Conclusions

The present study addressed how VO_x concentration in water-granulated EAF slags influenced the structure of the vitrified fraction and the consequent SCM reactivity, finding that:

- Increasing VO_x drove saturation of the RO solid solution, promoted spinel crystallization, and shifted C_2S crystallization to higher temperatures, altogether lowering the amorphous fraction of the slag, reaching a plateau at the highest VO_x concentrations.
- Vanadium added as V_2O_3 in the slag synthesis followed a valence redistribution; a portion of vanadium adopted network-forming roles, as indicated by Raman features consistent with higher valence vanadium in the vitrified fraction.
- Despite this, the vitrified slag was net-depolymerized—suggested to be driven by the redox balance formed with iron.
- Consequently, increasing VO_x systematically enhanced the inherent SCM reactivity, possibly owing to the depolymerization of the glass network in combination with no new inner diffusion barriers introduced by vanadium during slag dissolution. Notably, this increase in reactivity occurred despite the reduction in amorphous fraction with increased VO_x content.

The implications of these findings suggest that vanadium distribution to EAF slags in the context of H-DRI is no concern for reactivity but must be investigated further in the context of environmental impact.

Author Contributions A. Andersson: Conceptualization, Methodology, Formal analysis, Investigation, Data curation, Writing—Original Draft, Writing—Review and Editing, Project administration, Funding acquisition. M.J. Lee: Investigation, Data curation. S.H. Park: Investigation, Data curation. S.M. Hwang: Investigation, Data curation. F. Engström: Writing—Review and Editing. J.H. Park: Formal analysis, Writing—Review and Editing, Project administration, Funding acquisition.

Funding Open access funding provided by Lulea University of Technology. This study was funded by both the Swedish Research Council Formas (grant no. 2024—00347) and by the Korea Institute of Energy Technology Evaluation and Planning (KETEP, Grant No. 20217510100080), funded by the Ministry of Trade, Industry and Energy (MOTIE), Korea. Furthermore, the study was conducted within the framework of CAMM, the Center for Advanced Mining and Metallurgy at Luleå University of Technology.

Data Availability Original data is available from the corresponding authors on reasonable request.

Declarations

Conflict of Interest The authors declare that they have no conflicts of interest.

Open Access This article is licensed under a Creative Commons Attribution 4.0 International License, which permits use, sharing, adaptation, distribution and reproduction in any medium or format, as long as you give appropriate credit to the original author(s) and the source, provide a link to the Creative Commons licence, and indicate if changes were made. The images or other third party material in this article are included in the article's Creative Commons licence, unless indicated otherwise in a credit line to the material. If material is not included in the article's Creative Commons licence and your intended use is not permitted by statutory regulation or exceeds the permitted use, you will need to obtain permission directly from the copyright holder. To view a copy of this licence, visit <http://creativecommons.org/licenses/by/4.0/>.

References

1. Whittle JW, Rihner MCS, Hafez H, Espinosa RME, Fletcher DI, Walkley B, Koh LSC (2026) From symbiosis to scarcity: evaluating disruption associated with decarbonisation to circular waste materials between the UK cement and steel sectors. *Resour Conserv Recycl* 224:108560. <https://doi.org/10.1016/j.resconrec.2025.108560>
2. Ehrenberg A (2025) The steelmaking transformation process and its consequences for slag utilization. *Steel Res Int* 96:2400234. <https://doi.org/10.1002/srin.202400234>
3. Strandkvist I, Pålsson K, Andersson A, Olofsson J, Lennartsson A, Samuelsson C, Engström F (2020) Minimizing chromium leaching from low-alloy electric arc furnace (EAF) slag by adjusting the basicity and cooling rate to control brownmillerite formation. *Appl Sci* 10:35. <https://doi.org/10.3390/app10010035>
4. Mombelli D, Mapelli C, Gruttadauria A, Baldizzone C, Magni F, Levrangi PL, Simone P (2012) Analysis of electric arc furnace slag. *Steel Res Int* 83:1012–1019. <https://doi.org/10.1002/srin.201100259>
5. Lothenbach B, Scrivener K, Hooton RD (2011) Supplementary cementitious materials. *Cem Concr Res* 41:1244–1256. <https://doi.org/10.1016/j.cemconres.2010.12.001>
6. Kucharczyk S, Sitarz M, Zajac M, Deja J (2018) The effect of CaO/SiO_2 molar ratio of $\text{CaO}-\text{Al}_2\text{O}_3-\text{SiO}_2$ glasses on their structure and reactivity in alkali activated system. *Spectrochim Acta A Mol Biomol Spectrosc* 194:163–171. <https://doi.org/10.1016/j.saa.2018.01.018>
7. Glosser D, Suraneni P, Isgor OB, Weiss WJ (2021) Using glass content to determine the reactivity of fly ash for thermodynamic calculations. *Cem Concr Compos* 115:103849. <https://doi.org/10.1016/j.cemconcomp.2020.103849>
8. Snellings R (2013) Solution-controlled dissolution of supplementary cementitious material glasses at pH 13: the effect of solution composition on glass dissolution rates. *J Am Ceram Soc* 96:2467–2475. <https://doi.org/10.1111/jace.12480>
9. Skibsted J, Snellings R (2019) Reactivity of supplementary cementitious materials (SCMs) in cement blends. *Cem Concr Res* 124:105799. <https://doi.org/10.1016/j.cemconres.2019.105799>
10. Schöler A, Winnefeld F, Haha MB, Lothenbach B (2017) The effect of glass composition on the reactivity of synthetic glasses. *J Am Ceram Soc* 100:2553–2567. <https://doi.org/10.1111/jace.14759>


11. Lu X, Dai W, Liu X, Cang D, Zhou L (2019) Effect of basicity on cementitious activity of modified electric arc furnace steel slag. *Metall Res Technol* 116:217. <https://doi.org/10.1051/metal/2018069>
12. Yao Y, Wang Y, Wei Q, Cui S, Hao L (2020) Effect of the formation of amorphous networks on the structure and hydration characteristics of granulated blast furnace slag. *Materials (Basel)* 13:1462. <https://doi.org/10.3390/ma13061462>
13. Andersson A, Isaksson J, Lennartsson A, Roos Å, Engström F (2025) The role of FeO/SiO₂ ratio in valorizing iron silicate slags as supplementary cementitious materials. *J Sustain Metall* 11:657–669. <https://doi.org/10.1007/s40831-025-01022-5>
14. Ramanathan S, Perumal P, Illikainen M, Suraneni P (2021) Mechanically activated mine tailings for use as supplementary cementitious materials. *RILEM Tech Lett* 6:61–69. <https://doi.org/10.21809/rilemtechlett.2021.143>
15. Ramanathan S, Tuen M, Suraneni P (2022) Influence of supplementary cementitious material and filler fineness on their reactivity in model systems and cementitious pastes. *Mater Struct* 55:136. <https://doi.org/10.1617/s11527-022-01980-2>
16. Ehrenberg A, Romero Sarcos N, Hart D, Bornhöft H, Deubener J (2020) Influence of the thermal history of granulated blast furnace slags on their latent hydraulic reactivity in cementitious systems. *J Sustain Metall* 6:207–215. <https://doi.org/10.1007/s40831-020-00269-4>
17. Pronina N, Krüger S, Bornhöft H, Deubener J, Ehrenberg A (2018) Cooling history of a wet-granulated blast furnace slag (GBS). *J Non Cryst Solids* 499:344–349. <https://doi.org/10.1016/j.jnoncrsol.2018.07.054>
18. Kim HS, Kim KS, Jung SS, Hwang JI, Choi JS, Sohn I (2015) Valorization of electric arc furnace primary steelmaking slags for cement applications. *Waste Manage* 41:85–93. <https://doi.org/10.1016/j.wasman.2015.03.019>
19. Bullerjahn F, Bolte G (2022) Composition of the reactivity of engineered slags from bauxite residue and steel slag smelting and use as SCM for Portland cement. *Constr Build Mater* 321:126331. <https://doi.org/10.1016/j.conbuildmat.2022.126331>
20. Andersson A, Isaksson J, Lennartsson A, Engström F (2024) Insights into the valorization of electric arc furnace slags as supplementary cementitious materials. *J Sustain Metall* 10:96–109. <https://doi.org/10.1007/s40831-023-00778-y>
21. Muhmood L, Vitta S, Venkateswaran D (2009) Cementitious and pozzolanic behavior of electric arc furnace steel slags. *Cem Concr Res* 39:102–109. <https://doi.org/10.1016/j.cemconres.2008.11.002>
22. Rojas MF, Sánchez De Rojas MI (2004) Chemical assessment of the electric arc furnace slag as construction material: expansive compounds. *Cem Concr Res* 34:1881–1888. <https://doi.org/10.1016/j.cemconres.2004.01.029>
23. Hekal EE, Abo-El-Enein SA, El-Korashy SA, Megahed GM, El-Sayed TM (2013) Hydration characteristics of Portland cement–electric arc furnace slag blends. *HBRC J* 9:118–124. <https://doi.org/10.1016/j.hbrcj.2013.05.006>
24. Alsheltat MF, Elfigh MA (2023) Effects of electric arc furnace slag powder and fly ash within ternary waste blend on performance of concrete. *Open Ceram* 14:100359. <https://doi.org/10.1016/j.oceram.2023.100359>
25. Lee JY, Choi JS, Yuan TF, Yoon YS, Mitchell D (2019) Comparing properties of concrete containing electric arc furnace slag and granulated blast furnace slag. *Materials (Basel)* 12:1371. <https://doi.org/10.3390/ma12091371>
26. Amin MS, El-Gamal SMA, Abo-El-Enein SA, El-Hosiny FI, Ramadan M (2015) Physico-chemical characteristics of blended cement pastes containing electric arc furnace slag with and without silica fume. *HBRC J* 11:321–327. <https://doi.org/10.1016/j.hbrcj.2014.07.002>
27. Roslan NH, Ismail M, Abdul-Majid Z, Ghoreishiamiri S, Muhammad B (2016) Performance of steel slag and steel sludge in concrete. *Constr Build Mater* 104:16–24. <https://doi.org/10.1016/j.conbuildmat.2015.12.008>
28. Bonfante F, Ferrara G, Humbert P, Garufi D, Tulliani JM, Palmero P (2025) Aqueous carbonation of EAF steel slag to produce supplementary cementitious material: effects on mineral composition, hydration reactivity and mechanical properties. *Constr Build Mater* 479:141361. <https://doi.org/10.1016/j.conbuildmat.2025.141361>
29. Chandel SS, Lavakumar A, Randhawa NS, Singh PK (2025) Unique hot stage modification technique to enhance cementitious properties of electric arc furnace steel slag. *J Environ Manage* 376:124398. <https://doi.org/10.1016/j.jenvman.2025.124398>
30. Kallio R, Cantaluppi M, Louhisalmi J, Visuri VV (2025) Mineralogical characteristics of fossil-free steel slags. *Miner Eng* 230:109396. <https://doi.org/10.1016/j.mineng.2025.109396>
31. Lund C (2013) Mineralogical, chemical and textural characterisation of the malMBERGET iron ore deposit for a geometallurgical model. Doctoral Thesis, Luleå University of Technology
32. Heo J, Lee Y, Park H, Park JH (2021) Influence of slag composition and oxygen potential on thermodynamic behavior of vanadium in FeO-TiO₂-MgO-SiO₂-Al₂O₃ smelting slag and molten iron. *J Mater Res Technol* 15:5723–5732. <https://doi.org/10.1016/j.jmrt.2021.11.035>
33. Park D, Jung JS, Lee J (2023) Thermodynamic investigation of vanadium oxide in CaO–SiO₂–VO_x system at 1873 K. *J Am Ceram Soc* 106:767–779. <https://doi.org/10.1111/jace.18788>
34. Wang H, Wang L, Seetharaman S (2016) Determination of vanadium oxidation states in CaO-MgO-Al₂O₃-SiO₂-VO_x system by K Edge XANES method. *Steel Res Int* 87:199–209. <https://doi.org/10.1002/srin.201500256>
35. Wang L, Teng L, Chou KC, Seetharaman S (2013) Determination of vanadium valence state in CaO-MgO-Al₂O₃-SiO₂ system by high-temperature mass spectrometry. *Metall Mater Trans B* 44:948–953. <https://doi.org/10.1007/s11663-013-9836-6>
36. Farah H, Brungs M (2003) Oxidation-reduction equilibria of vanadium in CaO-SiO₂, CaO-Al₂O₃-SiO₂ and CaO-MgO-SiO₂ melts. *J Mater Sci* 38:1885–1894. <https://doi.org/10.1023/A:1023588010572>
37. Mittelstädt R, Schwerdtfeger K (1990) The dependence of the oxidation state of vanadium on the oxygen pressure in melts of VO_x, Na₂O-VO_x, and CaO-SiO₂-VO_x. *Metall Mater Trans B* 21:111–120. <https://doi.org/10.1007/BF02658122>
38. Inoue R, Suito H (1982) Distribution of vanadium between liquid iron and MgO-saturated slags of the system CaO-MgO-FeO_x-SiO₂. *Tetsu-to-Hagane* 68:54–62. https://doi.org/10.2355/tetsu-tohagane1955.68.10_1532
39. Xie X, Liu C, Qiu J, Li W, Huo G (2025) Phase equilibrium of CaO–Al₂O₃–VO_x system in air atmosphere at 1400 °C. *Metall Mater Trans B* 56:2982–2992. <https://doi.org/10.1007/s11663-025-03537-4>
40. Liu C, Xie X, Qiu J, Li W, Huo G (2024) The phase diagram of a CaO-Al₂O₃-VO_x slag system under argon atmosphere at 1500 °C. *Metals* 14:108. <https://doi.org/10.3390/met14010108>
41. Liu C, Xie X, Qiu J, Li W, Huo G (2024) Phase diagram of CaO-Al₂O₃-VO_x slag system under reducing atmosphere. *JOM* 76:6555–6567. <https://doi.org/10.1007/s11837-024-06866-y>
42. Kerkouri N, Haddad M, Et-Tabirou M, Chahine A, Laânaab L (2011) FTIR, Raman, EPR and optical absorption spectral studies on V₂O₅-doped cadmium phosphate glasses. *Physica B Condens Matter* 406:3142–3148. <https://doi.org/10.1016/j.physb.2011.04.057>

43. Sengupta P, Dey KK, Halder R, Ajithkumar TG, Abraham G, Mishra RK, Kaushik CP, Dey GK (2015) Vanadium in borosilicate glass. *J Am Ceram Soc* 98:88–96. <https://doi.org/10.1111/jace.13303>
44. McKeown DA, Gan H, Pegg IL (2017) X-ray absorption and Raman spectroscopy studies of molybdenum environments in borosilicate waste glasses. *J Nucl Mater* 488:143–149. <https://doi.org/10.1016/j.jnucmat.2017.03.012>
45. Tricot G, Montagne L, Delevoye L, Palavit G, Kostoj V (2004) Redox and structure of sodium-vanadophosphate glasses. *J Non-Cryst Solids* 345–346:56–60. <https://doi.org/10.1016/j.jnoncrystol.2004.07.043>
46. Lu X, Deng L, Saslow SA, Liu H, Benmore CJ, Parruzot BP, Reiser JT, Kim SH, Ryan JV, Vienna JD, Du J (2021) Vanadium oxidation states and structural role in aluminoborosilicate glasses: an integrated experimental and molecular dynamics simulation study. *J Phys Chem B* 125:12365–12377. <https://doi.org/10.1021/acs.jpcc.1c07134>
47. Chen Q (2020) Optical linear & nonlinearity and Faraday rotation study on V₂O₅ nanorod doped glass and glass-ceramic: impact of optical basicity. *J Alloys Compd* 836:155490. <https://doi.org/10.1016/j.jallcom.2020.155490>
48. Attos O, Massot M, Balkanski M, Haro-Poniatowski E, Asomoza M (1997) Structure of borovanadate glasses studied by Raman spectroscopy. *J Non-Cryst Solids* 210:163–170. [https://doi.org/10.1016/S0022-3093\(96\)00596-0](https://doi.org/10.1016/S0022-3093(96)00596-0)
49. Bersani D, Antonioli G, Lottici PP, Dimitriev Y, Dimitrov V, Kobourova P (1998) Coordination changes in telluro-vanadate glasses containing ZnO or CdO. *J Non-Cryst Solids* 232–234:293–299. [https://doi.org/10.1016/S0022-3093\(98\)00494-3](https://doi.org/10.1016/S0022-3093(98)00494-3)
50. Hübert T, Mosel G, Witke K (2001) Structural elements in borovanadate glasses. *Glass Phys Chem* 27:114–120. <https://doi.org/10.1023/A:1011376225695>
51. Ardelean I, Rusu D, Andronache C, Ciobotă V (2007) Raman study of xMeO·(100-x)[P₂O₅-Li₂O] (MeO ⇒ Fe₂O₃ or V₂O₅) glass systems. *Mater Lett* 61:3301–3304. <https://doi.org/10.1016/j.matlet.2006.11.057>
52. Manara D, Grandjean A, Pinet O, Dussosoy JL, Neuville DR (2007) Sulfur behavior in silicate glasses and melts: implications for sulfate incorporation in nuclear waste glasses as a function of alkali cation and V₂O₅ content. *J Non-Cryst Solids* 353:12–23. <https://doi.org/10.1016/j.jnoncrystol.2006.09.041>
53. Vedeanu N, Cozar O, Ardelean I, Lendl B, Magdas DA (2008) Raman spectroscopic study of CuO-V₂O₅-P₂O₅-CaO glass system. *Vib Spectrosc* 48:259–262. <https://doi.org/10.1016/j.vibspec.2008.01.003>
54. Cicconi MR, Lu Z, Uesbeck T, van Wüllen L, Brauer DS, de Ligny D (2020) Influence of vanadium on optical and mechanical properties of aluminosilicate glasses. *Front Mater* 7:161. <https://doi.org/10.3389/fmats.2020.00161>
55. Laorodphan N, Pooddee P, Kidkhunthod P, Kunthadee P, Tapala W, Puntharod R (2016) Boron and pentavalent vanadium local environments in binary vanadium borate glasses. *J Non Cryst Solids* 453:118–124. <https://doi.org/10.1016/j.jnoncrystol.2016.10.005>
56. Li Y, Liang K, Cao J, Xu B (2010) Spectroscopy and structural state of V⁴⁺ ions in lithium aluminosilicate glass and glass-ceramics. *J Non Cryst Solids* 356:502–508. <https://doi.org/10.1016/j.jnoncrystol.2009.12.018>
57. Li Y, Cao J, Xu B, Liang K (2011) Spectroscopic study of optical property and structural state of vanadium ions in lithium aluminosilicate glass-ceramics. *Spectrosc Lett* 44:67–76. <https://doi.org/10.1080/00387010903512855>
58. Neeraja K, Rao TGVM, Kumar AR, Uma Lakshmi V, Veeraiyah N, Rami Reddy M (2013) Spectroscopic properties of Sm³⁺ and V⁴⁺ ions in Na₂O-SiO₂-ZrO₂ glasses. *J Mol Struct* 1054–1055:339–348. <https://doi.org/10.1016/j.molstruc.2013.09.038>
59. Vedeanu N, Cozar O, Ardelean I, Filip S (2006) Spectroscopic investigation on some calcium-phosphate glasses. *J Optoelectron Adv Mater* 8:1135–1139
60. Smith-Gray N, Lonergan J, McCloy J (2021) Chromium and vanadium incorporation in sulfate-containing sodium aluminoborosilicate glass. *MRS Adv* 6:138–148. <https://doi.org/10.1557/s43580-021-00034-z>
61. Donatini A, Georges P, Fevre T, Cormier L, Neuville DR (2025) Deciphering vanadium redox and structure in aluminosilicate glass: a spectroscopic study. *J Non Cryst Solids* 666:123689. <https://doi.org/10.1016/j.jnoncrystol.2025.123689>
62. Bale CW, Bélisle E, Chartrand P, Deckerov SA, Eriksson G, Gheribi AE, Hack K, Jung IH, Kang YB, Melançon J, Pelton AD, Petersen S, Robelin C, Sangster J, Spencer P, Van Ende MA (2016) Reprint of: FactSage thermochemical software and databases, 2010–2016. *Calphad* 55:1–19. <https://doi.org/10.1016/j.calphad.2016.07.004>
63. Hellenbrandt M (2004) The inorganic crystal structure database (ICSD) – Present and future. *Crystallogr Rev* 10:17–22. <https://doi.org/10.1080/08893110410001664882>
64. Zagorac D, Müller H, Ruehl S, Zagorac J, Rehme S (2019) Recent developments in the Inorganic Crystal Structure Database: theoretical crystal structure data and related features. *J Appl Crystallogr* 52:918–925. <https://doi.org/10.1107/S160057671900997X>
65. Avet F, Snellings R, Diaz AA, Haha MB, Scrivener K (2016) Development of a new rapid, relevant and reliable (R3) test method to evaluate the pozzolanic reactivity of calcined kaolinitic clays. *Cem Concr Res* 85:1–11. <https://doi.org/10.1016/j.cemconres.2016.02.015>
66. Li X, Snellings R, Antoni M, Alderete NM, Haha MB, Bishnoi S, Cizer Ö, Cyr M, De Weerd K, Dhandapani Y, Duchesne J, Haufe J, Hooton D, Juenger M, Kamali-Bernard S, Kramar S, Marroccoli M, Joseph AM, Parashar A, Patapy C, Provis JL, Sabio S, Santhanam M, Steger L, Sui T, Telesca A, Vollpracht A, Vargas F, Walkley B, Winnefeld F, Ye G, Zajac M, Zhang S, Scrivener KL (2018) Reactivity tests for supplementary cementitious materials: RILEM TC 267-TRM phase 1. *Mater Struct* 51:1–14. <https://doi.org/10.1617/s11527-018-1269-x>
67. Hallet V, De Belie N, Pontikes Y (2020) The impact of slag fineness on the reactivity of blended cements with high-volume non-ferrous metallurgy slag. *Constr Build Mater* 257:119400. <https://doi.org/10.1016/j.conbuildmat.2020.119400>
68. Sivakumar PP, Matthys S, De Belie N, Gruyaert E (2021) Reactivity assessment of modified ferro silicate slag by R3 method. *Appl Sci Basel* 11:366. <https://doi.org/10.3390/app11010366>
69. Allibert M (1995) Slag atlas, 2nd edn. Verlag Stahleisen GmbH, Düsseldorf, p 63
70. Wang Y, Zhang R, Zhao X, Min Y, Liu C (2020) Structural transformation of molten CaO-SiO₂-Al₂O₃-Fe_xO slags during secondary refining of steels. *ISIJ Int* 60:220–225. <https://doi.org/10.2355/isijinternational.ISIJINT-2019-418>
71. Das S, Madheshiya A, Ghosh M, Dey KK, Gautam SS, Singh J, Mishra R, Gautam C (2019) Structural, optical, and nuclear magnetic resonance studies of V₂O₅-doped lead calcium titanate borosilicate glasses. *J Phys Chem Solids* 126:17–26. <https://doi.org/10.1016/j.jpcs.2018.10.030>
72. Kim TS, Park JH (2020) Thermodynamics of iron redox equilibria and viscosity-structure relationship of CaO-Al₂O₃-Fe_xO melts. *J Non-Cryst Solids* 542:120089. <https://doi.org/10.1016/j.jnoncrystol.2020.120089>
73. Wen Y, Shu Q, Lin Y, Fabritius T (2023) Effect of SiO₂ content and mass ratio of CaO to Al₂O₃ on the viscosity and structure of

- CaO–Al₂O₃–B₂O₃–SiO₂ slags. *ISIJ Int* 63:1–9. <https://doi.org/10.2355/isijinternational.ISIJINT-2022-288>
74. Kim TS, Park JH (2021) Viscosity-structure relationship of CaO–Al₂O₃–Fe₂O₃–SiO₂–MgO Ruhrstahl-Heraeus (RH) refining slags. *ISIJ Int* 61:724–733. <https://doi.org/10.2355/ISIJINTERNATIONAL.ISIJINT-2020-482>
 75. Pu J, Gao L, Yang Z, Kang J, Zhang M, Ruan R, Peng J, Chen G (2020) The application of microwave irradiation technology on the preparation of V₂O₅ from ammonium polyvanadate (APV). *J Taiwan Inst Chem Eng* 109:1–7. <https://doi.org/10.1016/j.jtice.2020.02.010>
 76. Zhang L, Chen M, Sun X (2022) Evolution of viscosity and structure property during aluminothermic reduction of vanadium-enriched slag. *Steel Res Int* 93:2100738. <https://doi.org/10.1002/srin.202100738>
 77. Zhang L, Chen M, Wang N, Huang M (2021) Evolution of viscosity and structure property of vanadium slag during iron-extracting reduction process. *steel res int* 92:2000501. <https://doi.org/10.1002/srin.202000501>
 78. Huang WJ, Zhao YH, Yu S, Zhang LX, Ye ZC, Wang N, Chen M (2016) Viscosity property and structure analysis of FeO–SiO₂–V₂O₅–TiO₂–Cr₂O₃ slags. *ISIJ Int* 56:594–601. <https://doi.org/10.2355/isijinternational.ISIJINT-2015-457>
 79. Zhang R, Wang Y, Zhao X, Jia J, Liu C, Min Y (2020) Structure and viscosity of molten CaO–SiO₂–Fe_xO slag during the early period of basic oxygen steelmaking. *Metall Mater Trans B* 51:2021–2029. <https://doi.org/10.1007/s11663-020-01888-8>
 80. Xu R, Wang Z (2025) Structural characteristics and viscous behaviors of Al₂O₃–CaO–SiO₂–Fe₂O₃ slags. *Int J Miner Metall Mater* 32:1068–1078. <https://doi.org/10.1007/s12613-024-3078-2>
 81. Whittaker L, Velazquez JM, Banerjee S (2011) A VO-seeded approach for the growth of star-shaped VO₂ and V₂O₅ nanocrystals: facile synthesis, structural characterization, and elucidation of electronic structure. *CrystEngComm* 13:5328–5336. <https://doi.org/10.1039/c0ce00832j>
 82. Shvets P, Dikaya O, Maksimova K, Goikhman A (2019) A review of Raman spectroscopy of vanadium oxides. *J Raman Spectrosc* 50:1226–1244. <https://doi.org/10.1002/jrs.5616>
 83. Xin J, Wang N, Chen M, Lv X (2022) Viscosity and structure evolution of molten vanadium slag during carbothermic reduction process. *J Non-Cryst Solids* 595:121840. <https://doi.org/10.1016/j.jnoncrysol.2022.121840>
 84. Fang X, Zhang F, Zheng T, Lv J, Zhang J, Guo Y (2022) Effect of Fe₂O₃ substitution of V₂O₅ on structure and electrical conductivity of lithium vanadium phosphate glass. *J Non-Cryst Solids* 586:121571. <https://doi.org/10.1016/j.jnoncrysol.2022.121571>
 85. Moisiu C, Curran MD, Van De Burt LJ, Stiegman AE (2005) Raman spectroscopy of discrete silica supported vanadium oxide: assignment of fundamental stretching modes. *J Mater Chem* 15:3519–3524. <https://doi.org/10.1039/b505661f>
 86. Shen X, Chen M, Wang N, Wang D (2019) Viscosity property and melt structure of CaO–MgO–SiO₂–Al₂O₃–FeO slag system. *ISIJ Int* 59:9–15. <https://doi.org/10.2355/isijinternational.ISIJINT-2018-479>
 87. Mysen BO, Finger LW, Virgo D, Seifert FA (1982) Curve-fitting of Raman spectra of silicate glasses. *Am Mineral* 67:686–695
 88. Kashio S, Iguchi Y, Goto T, Nishina Y, Fuwa T (1980) Raman spectroscopic study on the structure of silicate slag. *Trans ISIJ* 20:251–253. <https://doi.org/10.2355/isijinternational1966.20.251>
 89. Mysen BO, Virgo D, Scarfe CM (1980) Relations between the anionic structure and viscosity of silicate melts – A Raman spectroscopic study. *Am Mineral* 65:690–710
 90. Mysen BO, Virgo D (1989) Redox equilibria, structure, and properties of Fe-bearing aluminosilicate melts: relationships among temperature, composition, and oxygen fugacity in the system Na₂O–Al₂O₃–SiO₂–Fe–O. *Am Mineral* 74:58–76
 91. Nam SH, Park JH (2025) MgO solubility in Li₂O-containing iron-silicate slag at 1823 K: pyro-processing of secondary lithium-ion battery (LIB) sources. *Ceram Int*. <https://doi.org/10.1016/j.ceramint.2025.08.060>
 92. Åström E, Andersson A, Björkman B, Björkvall J (2025) Influence of vanadium oxide on the viscosity within the CaO–SiO₂–“FeO”–MgO system. *Metall Mater Trans B* 56:821–832. <https://doi.org/10.1007/s11663-024-03322-9>
 93. Terai R, Hayami R (1975) Ionic diffusion in glasses. *J Non Cryst Solids* 18:217–264
 94. Mazurek K, Białowicz K, Trypuć M (2010) Extraction of vanadium compounds from the used vanadium catalyst with the potassium hydroxide solution. *Pol J Chem Technol* 12:23–28. <https://doi.org/10.2478/v10026-010-0005-2>
 95. Singh N, Kang HN, Jyothi RK, Jha MK, Pasupuleti KS, Lee JY (2025) Hydrometallurgical approach to recover vanadium and aluminum from the sulfuric acid manufacturing spent catalyst. *Min Proc Ext Metall Rev* 46:865–876. <https://doi.org/10.1080/08827508.2025.2456027>
 96. Tan J, Wang J, Song Y, Liu Z, Liu M, Ling J, An H (2020) Research on separation and recovery of vanadium, molybdenum, aluminium in alkaline solution by chemical precipitation. *J Petrochem Univ* 33:13–18
 97. Andersson A, Brander L, Lennartsson A, Roos Å, Engström F (2023) A method for synthesizing iron silicate slags to evaluate their performance as supplementary cementitious materials. *Appl Sci* 13:8357. <https://doi.org/10.3390/app13148357>
 98. Sinyoung S, Kajitvichyanukul P (2015) Influence of vanadium on cement properties and leaching analysis. *Adv Mat Res* 1103:113–119. <https://doi.org/10.4028/www.scientific.net/amr.1103.113>
 99. Hillier SR, Sangha CM, Plunkett BA, Walden PJ (1999) Long-term leaching of toxic trace metals from Portland cement concrete. *Cem Concr Res* 29:515–521. [https://doi.org/10.1016/S0008-8846\(98\)00200-2](https://doi.org/10.1016/S0008-8846(98)00200-2)
 100. Vollpracht A, Brameshuber W (2016) Binding and leaching of trace elements in Portland cement pastes. *Cem Concr Res* 79:76–92. <https://doi.org/10.1016/j.cemconres.2015.08.002>
 101. Hartwich P, Vollpracht A (2017) Influence of leachate composition on the leaching behaviour of concrete. *Cem Concr Res* 100:423–434. <https://doi.org/10.1016/j.cemconres.2017.07.002>

Publisher's Note Springer Nature remains neutral with regard to jurisdictional claims in published maps and institutional affiliations.

Authors and Affiliations

Anton Andersson^{1,2}  · Min Joo Lee² · Sung Hwan Park² · Su Min Hwang² · Fredrik Engström¹ · Joo Hyun Park²

✉ Anton Andersson
anton.andersson@ltu.se

✉ Joo Hyun Park
basicity@hanyang.ac.kr

¹ Process Metallurgy, Luleå University of Technology,
971 87 Luleå, Sweden

² Department of Materials Science and Chemical Engineering,
Hanyang University, Ansan 155 88, Korea